PAPER

Check for updates

Cancer-targeting gold-decorated melanin nanoparticles for *in vivo* near-infrared photothermal therapy†

Ghasidit Pornnoppadol,‡[a] Soojeong Cho,‡[b] Jeong Heon Yu,‡[a] Shin-Hyun Kim [iD] *[b] and Yoon Sung Nam [iD] *[ac]

Photothermal cancer therapy has gained increasing attention as a minimally invasive treatment *via* the localized heating of photothermal agents to eradicate cancer cells. However, its clinical translation has been limited by insufficient photothermal conversion in the near-infrared (NIR) range and low tumor-targeting efficiency. Here, synthetic melanin-like nanoparticles (~190 nm in diameter) decorated with a cluster of smaller gold nanoparticles (~20 nm in diameter) are developed as efficient NIR photothermal agents for *in vivo* cancer treatment. The melanin-gold hybrid nanoparticles are prepared by the oxidative polymerization of dopamine into colloidal melanin-like nanoparticles, followed by the spontaneous reduction of gold ion precursors into plasmonic nanoparticles on the surface of melanin nanoparticles. The gold nanoparticles significantly increase the NIR light absorption and photothermal conversion of the melanin nanoparticles, making their overall photothermal performance superior to conventional gold nanorods. Chemical conjugation of epidermal growth factor to the hybrid nanoparticles facilitates their cellular internalization into lung adenocarcinoma cells and enables *in vivo* tumor-targeting in a xenograft mouse model. The nanoparticles also exhibit excellent dispersion stability in serum and maintain high photothermal efficiency even after extensive laser irradiation. Our results suggest that the electronic hybridization of melanin and gold nanostructures provides a new opportunity to fine-tune their optical and chemical properties for tumor-targeted photothermal therapy.

Design, System, Application

This work proposes a cancer-targeting near-infrared (NIR) photothermal nanomaterial prepared by hybridizing melanin-like nanoparticles having an average diameter of 190 nm with a cluster of ~20 nm gold nanoparticles and conjugating targeting ligands to the nanoparticle surface with a polyethylene glycol spacer. The absorption spectrum and photothermal conversion efficiency can be adjusted by controlling the particle sizes and surface density of gold nanoparticles. Structural robustness, efficient cellular uptake, and biocompatibility of the hybrid photothermal nanomaterial can find its immediate application for hyperthermia cancer treatment.

Introduction

Photothermal therapy, which uses light-induced localized heating to kill abnormal cells, provides minimal invasiveness and high selectivity of cells, thereby serving as a promising means to treat cancers. During therapy, photothermal nanoparticles convert light to thermal energy, increasing the local temperature around the nanoparticles. The heat causes cell death when the temperature is raised above 42–48 °C.[1,2] Because near-infrared (NIR) light in the wavelength range of 650–950 nm can penetrate the skin and tissues of 1–2 cm thickness, NIR-active photothermal agents are much more useful than visible light-based ones to treat tumors located beneath the skin.[3–5]

There are various types of photothermal agents, including organic dyes, carbon nanomaterials, metal nanoparticles, and quantum dots.[3,6–10] In particular, plasmonic gold nanostructures with various shapes have been widely investigated for photothermal effects due to their unique optical properties, structural and spectral tunability, and

[a] Department of Materials Science and Engineering, Korea Advanced Institute of Science and Technology, 291 Daehak-ro, Yuseong-gu, Daejeon 34141, Republic of Korea. E-mail: yoonsung@kaist.ac.kr

[b] Department of Chemical and Biomolecular Engineering, Korea Advanced Institute of Science and Technology, 291 Daehak-ro, Yuseong-gu, Daejeon 34141, Republic of Korea. E-mail: kim.sh@kaist.ac.kr

[c] Department of Biological Sciences, Korea Advanced Institute of Science and Technology, 291 Daehak-ro, Yuseong-gu, Daejeon 34141, Republic of Korea

† Electronic supplementary information (ESI) available. See DOI: https://doi.org/10.1039/d3me00173c

‡ These authors equally contributed to this work.

This journal is © The Royal Society of Chemistry and IChemE 2024

Mol. Syst. Des. Eng., 2024, **9**, 507–517 | **507**

biocompatibility.[3,8–10] Gold nanorods (AuNRs) exhibit strong plasmon resonances in the NIR range, which reduces absorption and scattering by the biological medium and enables efficient heat generation, making AuNRs a viable candidate as a photothermal agent.[9] Nevertheless, their practical applications are limited by several technical problems, including poor production controllability in terms of monodispersity, scaling, and purity.[10] They also exhibit a low cellular internalization efficiency, at least three-fold less than spherical gold nanoparticles (AuNPs), which reduces therapeutic effectiveness.[11] The clinical application of other photothermal agents is also restricted by low photothermal conversion efficiency, cytotoxicity, and photochemical instability.

Colloidal melanin-like nanoparticles (MNPs), also called polydopamine nanoparticles, were suggested as a new promising photothermal agent as they exhibit a high photothermal conversion efficiency, ~40%, which is even higher than that of AuNRs.[12,13] Also, MNPs can maintain high structural stability under continuous light illumination and high dispersion stability in the blood. Their synthesis and surface modification routes are straightforward due to the abundant functional groups available for polymerization and chemical conjugation.[14,15] Although the NIR light absorption of MNPs is relatively higher than other photothermal agents, their light absorption is still mainly limited to the visible light range without any distinctive absorption mechanisms in the NIR spectrum. Spectral extension to a longer range has been attempted to improve the photothermal properties of MNPs through encapsulation and hybridization. For instance, microwave thermal therapy with hollow MNPs of 140 nm in diameter was suggested, but they were only effective with the help of ionic liquid as a sensitizer.[16] Several studies reported improved photothermal therapeutic effects through the surface coating of gold nanostructures with polydopamine.[17–19] Gold hollow superparticles were self-assembled from polydopamine-capped AuNPs of ~25 nm in diameter,[17] inducing a strong plasmon resonance coupling effect and an excellent photothermal conversion efficiency.[7] Polydopamine coatings of AuNRs also provide chemical functionality for surface modifications to incorporate therapeutic agents, probes, and targeting molecules.[18,19] However, in the previous works, polydopamine is contributed as an adhesive molecule, but not a primary photothermal agent. Considering the above-mentioned advantages of MNPs, we decided to focus on boosting the photothermal effect of MNPs by employing AuNPs as a supporting partner to increase the optical cross-section in the NIR range while maintaining their excellent structural stability and chemical versatility. Particularly, the surface functionality of MNPs allows us to harness them as a template for the formation of metal nanostructures, as observed in biomineralization processes.[20–24]

In this study, an efficient NIR photothermal agent was developed by functionalizing MNPs with a cluster of AuNPs through *in situ* surface synthesis. Surface active groups, such as hydroxyl and amine, of MNPs, enabled gold ion-catechol complexation and the spontaneous reduction of gold ions into solid AuNPs on the surface of the MNPs (denoted by 'Au-MNPs').[22–26] Importantly, the impact of clustering AuNPs on the NIR light absorption and photothermal conversion efficiency was investigated.[7,27] The structural and spectral stabilities of the Au-MNPs were also examined. The surface of the assembled nanostructures was chemically modified with epidermal growth factor (EGF) to enhance their tumor-targeting capabilities and cellular internalization. *In vitro* and *in vivo* photothermal effects of the Au-MNPs were examined using A549 adenocarcinoma human alveolar basal epithelial cells and a xenograft mouse model.

Results and discussion

Monodisperse MNPs were synthesized through oxidative polymerization by following the previously reported procedures.[12–15] Dopamine precursors were polymerized to spherical MNPs in a basic solution. A gold precursor, chloroauric acid ($HAuCl_4$), was added to the suspension of MNPs, as illustrated in Fig. 1a. The anionic precursors can be attracted by amine and catechol groups on the surface of MNPs.[25,28,29] The gold precursors were reduced to form AuNPs on the surface of MNPs, which serve as a mild reducing agent (the reducing potential of −0.434 eV) in the absence of additional reducing agents.[30] For the controlled surface synthesis of AuNPs on the MNPs, $HAuCl_4$ was slowly but steadily injected into a dispersion of MNPs to avoid rapid self-seeding and growth of AuNPs (see Fig. S1 of the ESI†). The coverage and size of AuNPs on MNPs increased with the increased concentration of $HAuCl_4$, (Fig. 1b). The coverage was as much as ~99%, and the diameter of AuNPs was 27 nm at a concentration of 10 mM of $HAuCl_4$. We utilized AuNP-free MNPs with a diameter of 190 nm and Au-MNPs assembled with AuNPs with a diameter of 20 nm for materials characterization and the comparison of photothermal effects (Fig. 1c).

AuNP-free MNPs show a broad range of absorption from UV to NIR, as represented by a black curve in Fig. 2a. In contrast, AuNP-decorated MNPs (denoted by 'Au-MNPs') exhibit a distinctive peak around 550 nm from the plasmonic resonance of AuNPs (represented by a red curve), indicating the successful formation of AuNPs on MNPs. The individual Au-MNPs also exhibit bright red colors under dark-field illumination due to the plasmonic effect of AuNPs, as shown in Fig. S2.† X-ray photoelectron (XP) spectroscopy further confirmed the on-surface synthesis of AuNPs: Au-MNPs had clear peaks at 84.0 eV and 353 eV for 4f and 4d orbitals of gold atoms, respectively, and a reduced peak at 398.1 eV for nitrogen, in comparison with MNPs (Fig. 2b). The atomic compositions of C, O, N, and Au are presented in Fig. S3.† The results indicate the formation of AuNPs through the reduction of amine derivatives. In addition, Fourier transform-infrared (FT-IR) spectroscopy shows the disappearance of the absorption band of N–H stretching vibration at 3357 cm^{-1} and that of –NH$_2$ bending at 1605 cm^{-1}, confirming the reduction of amine derivatives (Fig. 2c).

508 | *Mol. Syst. Des. Eng.*, 2024, **9**, 507–517

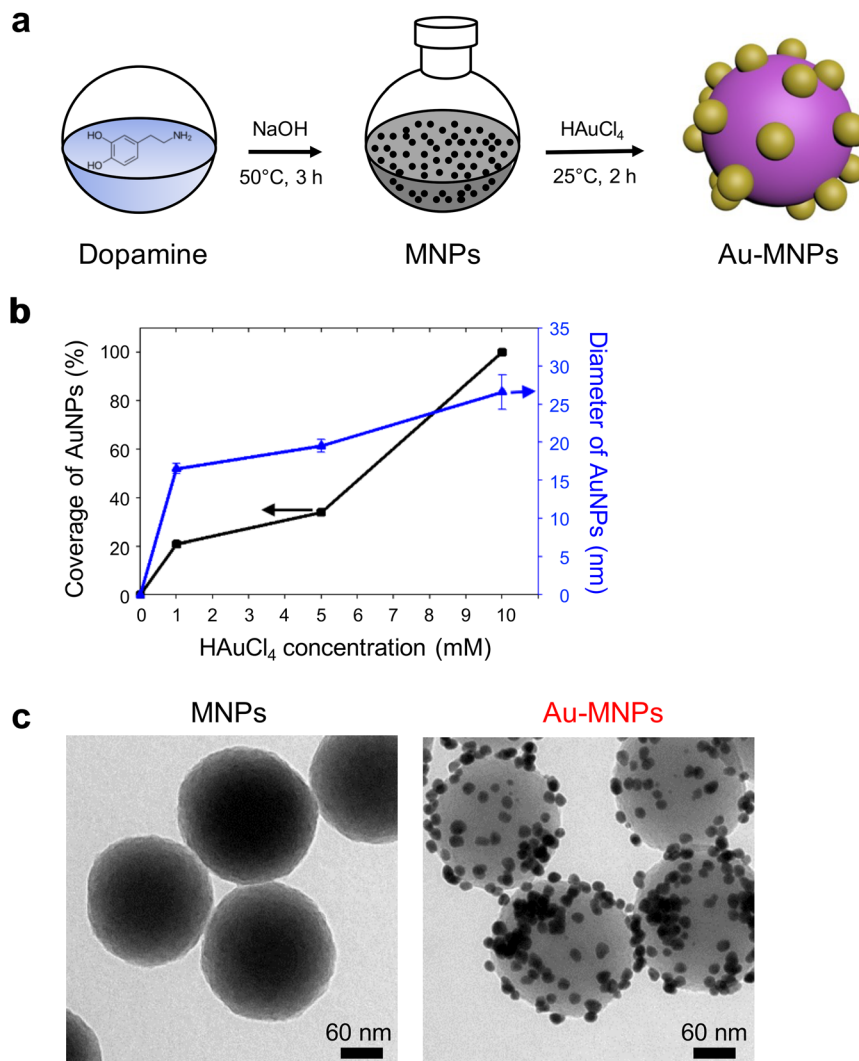This journal is © The Royal Society of Chemistry and IChemE 2024

Fig. 1 Synthesis of AuNP-decorated melanin-like nanoparticles. (a) Schematics of the synthesis of MNPs and subsequent surface functionalization with AuNPs: Dopamine is oxidatively polymerized in the presence of NaOH to form MNPs, and gold precursors are spontaneously reduced on the surface of MNPs to form Au-MNPs. (b) Influence of final concentration of gold precursors on the surface coverage and diameter of AuNPs on MNPs. (c) Transmission electron microscopy (TEM) images of MNPs (left) and Au-MNPs (right).

The surface functionalization of MNPs with a cluster of AuNPs increased the photothermal conversion efficiency. To compare the effect, we irradiated MNPs and Au-MNPs with the same weight fractions independently with an 808 nm laser with an intensity of 2.5 W cm^{-2} (Fig. S4†). The temperature increased upon heating and reached the maximum at a steady state. The difference, ΔT, between the maximum temperature and room temperature (25 °C) increased with the weight fraction, as shown in Fig. 3a. The difference for Au-MNPs was approximately 30% larger than that for Au-free MNPs, at the same weight fractions over the whole range. The increase in the temperature difference is noticeable at higher weight fractions. It exhibits a saturation curve as a function of concentration presumably due to the light-scattering properties of AuNPs. If the target ΔT is 40 °C, enough for photothermal therapy applications, the required weight concentration of Au-MNPs is less than half of MNPs. The reduced concentration of

the nanoparticles required for efficient photothermal effects is clinically important because the *in vivo* targeted delivery of photothermal agents is very challenging.

The photothermal conversion efficiency was estimated by a heating and cooling experiment (Fig. S5†).[31] For 0.8 wt% dispersions, MNPs and Au-MNPs exhibited efficiencies of 40% and 47%, respectively, much higher than polydopamine-coated AuNPs and AuNRs, 17–22%.[32,33] Note that our photothermal conversion efficiency for MNPs was the same as that of the previous one with a smaller diameter (160 nm) at a much lower particle concentration (0.02 wt%) under a lower intensity irradiation (2 W cm^{-2}).[12] As the conversion efficiency depends on the concentration, wavelength, and light intensity, the values must be compared under the same experimental conditions. Nevertheless, our MNPs certainly show a similar level of photothermal conversion efficiency as the previously reported MNPs. More importantly, Au-MNPs

Fig. 2 Characterization of gold–melanin nanoparticles. Absorption (a), X-ray photoelectron (XP) (b), and Fourier transform-infrared (FT-IR) (c) spectra of MNPs and Au-MNPs.

Fig. 3 (a) Concentration dependence of the difference between the maximum and room temperatures for the dispersions of MNPs and Au-MNPs. (b) Absorption spectra of Au-MNPs and a simple mixture of AuNPs and MNPs. Insets are TEM images of AuNPs, MNPs, and Au-MNPs. Scale bars are 50 nm. (c) Temporal change of temperature increase from room temperature for deionized water, the mixture of AuNPs and MNPs, and the dispersion of Au-MNPs during 808 nm laser irradiation with an intensity of 2.5 W cm^{-2}.

exhibited a significantly higher photoconversion efficiency than MNPs. In addition, AuNPs and AuNRs were synthesized for comparison as described in ESI, and their TEM images are shown in Fig. S6.† The photothermal conversion efficiencies of conventional AuNPs and AuNRs were 29% and
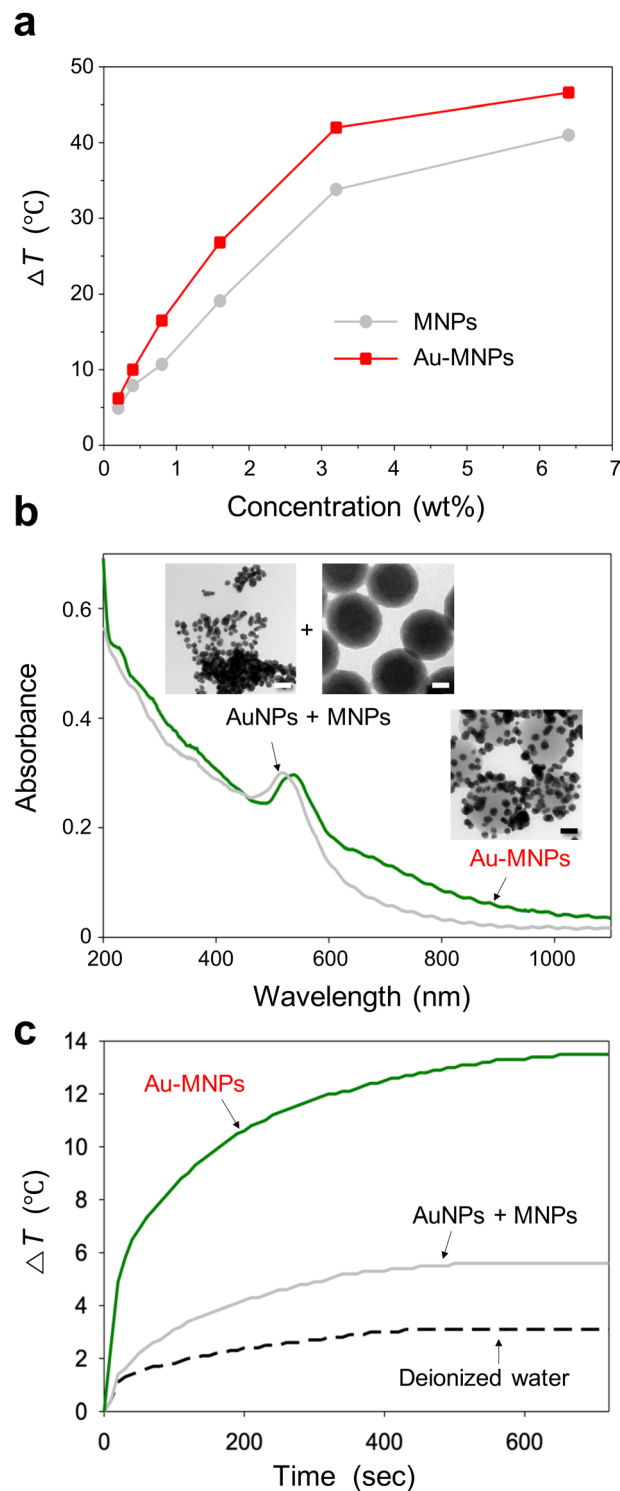
510 | *Mol. Syst. Des. Eng.*, 2024, **9**, 507–517

This journal is © The Royal Society of Chemistry and IChemE 2024

36%, respectively, comparable to the literature values (Fig. S7†).[34,35] The results indicate that Au-MNPs can convert light to heat significantly better than MNPs and AuNRs.

To study the origin of the higher maximum temperature and photothermal conversion efficiency of Au-MNPs *versus* MNPs, the absorption spectrum of Au-MNPs was compared with that of a simple mixture of MNPs and AuNPs with a diameter of 20 nm, which were synthesized separately (Fig. 3b). The concentration of MNPs was carefully adjusted to have an absorbance around 200–400 nm comparable to that of Au-MNPs, and that of AuNPs was also adjusted to have comparable absorbance around 550 nm, corresponding to the characteristic localized surface plasmon resonance (LSPR) wavelength. The absorbance of Au-MNPs significantly exceeded that of the simple mixture within the wavelength range of 600–1200 nm, indicating a pronounced enhancement in their optical properties in this region. In contrast, within the shorter wavelength spectrum of 200–550 nm, the absorbance levels of Au-MNPs and the simple mixture were found to be quite similar. Notably, at the wavelength of 808 nm, the absorbance value for Au-MNPs was found to be 2.67 times greater than that of the simple mixture. This substantial increase suggests the superior light-harvesting capability of Au-MNPs at this near-infrared wavelength, which is critically important for photothermal therapy. The observed difference in absorbance, particularly at 808 nm, is attributed to the phenomenon of coupled LSPR, which is facilitated by the close proximity of adjacent AuNPs within the Au-MNPs.[36,37] This coupling effect enhances the electromagnetic field at the nanoparticle surface, leading to a more efficient interaction with incident light. The induction of coupled LSPR is a distinctive feature of Au-MNPs, setting them apart from simpler nanoparticle mixtures, and is a key factor contributing to their enhanced photoconversion efficiency. Since the distance between AuNPs is not constant, a plurality of peaks from coupling modes are superimposed, therefore, resulting in an overall increase in absorbance. To compare heating activity further, the Au-MNP dispersion and the simple mixture, which had comparable absorbance in the range of 200–550 nm, were subjected to laser irradiation (Fig. 3c). The temperature increase from room temperature for Au-MNPs was 2.4 times higher than that of the simple mixture: a factor comparable to that of the absorbance enhancement. The Au-MNPs with high heating activity in the NIR region also satisfied the need for high structural and spectral stability. To prove this, the absorption spectra of Au-MNPs were obtained before and after laser irradiation for 30 min, as shown in Fig. S8.† The laser irradiation did not cause any significant changes in the spectra. In addition, the shape and structure of Au-MNPs remained unchanged during the laser irradiation, as shown in the inset.

With straightforward conjugation chemistry, EGF was attached as a cancer-targeting ligand to the surface of Au-MNPs using thiolated PEG, terminated with EGF, to form EGF-functionalized Au-MNP (denoted by 'ep-Au-MNP'), as illustrated in Fig. 4a. The thiolated PEG–EGF conjugates were prepared by the conjugation of carboxymethyl-PEG-thiol (CM–PEG–SH) to EGF by 1-ethyl-3-(3-dimethylaminopropyl) carbodiimide (EDC) and *N*-hydroxysuccinimide (NHS).[38] The PEG–EGF conjugate had a molecular weight of ~11 kDa because the CM–PEG–SH has a nominal molecular weight of 5 kDa, and EGF has a molecular weight of approximately 6.2 kDa, as determined by matrix-assisted laser desorption/ionization-time of flight (MALDI-TOF) analysis (Fig. S9†). In addition, the conjugation of CM–PEG–SH to EGF was further confirmed by reversed phase-high performance liquid chromatography (RP-HPLC) analysis, as shown in Fig. S10.† The thiolated PEG with EGF was then attached to the surface of the Au-MNPs with a coupling efficiency of ~97.5%. Although the thiol group can be linked to the catechol groups of MNPs, the Au surface might be the preferential conjugation site for the thiolated PEG because of the larger surface area and protruded structure of the AuNPs. For comparative studies, PEG-functionalized Au-MNPs without EGF (denoted by 'p-Au-MNPs') were also prepared. The hydrodynamic diameters of Au-MNPs, p-Au-MNPs, and ep-Au-MNPs were 201.8 ± 3.8 nm, 216.6 ± 6.1 nm, and 224.7 ± 4.3 nm, respectively, as estimated with dynamic light scattering (DLS) (Fig. S11a†). The zeta-potential of Au-MNPs was −36.17 ± 4.5 mV, and the conjugation with PEG reduced the potential to −15.29 ± 0.9 mV, as shown in Fig. S11b.† The conjugation with PEG–EGF yielded the potential of −23.81 ± 0.6 mV because EGF is negatively charged at a neutral pH. The conjugation with PEG and PEG–EGF did not cause any change in the absorption spectra, as shown in Fig. S11c.† The dispersions in 10% fetal bovine serum (FBS) in phosphate-buffered saline (PBS) maintained their stability during 12 h incubation at 37 °C, as confirmed by no significant change in hydrodynamic sizes (Fig. S11d†).

The cell cytotoxicities of Au-MNPs, p-Au-MNPs, and ep-Au-MNPs were evaluated with metastatic adenocarcinoma human alveolar basal epithelial cells (A549, 1×10^4 cells per well). The cell viability was measured using a cell counting kit-8 (CCK-8) assay. The results indicate that all three nanoparticles had no significant toxic responses throughout the range of the nanoparticle concentration (0–2 mg mL^{-1}), as shown in Fig. 4b. The cellular uptake of p-Au-MNPs and ep-Au-MNPs in A549 cells was observed under a dark-field microscope and quantified with inductively coupled plasma mass spectrometry (ICP-MS). The cells treated with p-Au-MNPs showed few red spots, whereas the cells treated with ep-Au-MNPs showed intensive red spots (Fig. 4c). This contrast indicates that EGF on Au-MNPs effectively binds to EGF receptors expressed on the A549 cell membrane and facilitates the cellular uptake. The average numbers of internalized ep-Au-MNPs per cell are about four times higher than that of p-Au-MNPs (Fig. 4d) (details of the calculation are described in ESI†). The high cellular uptake of ep-Au-MNPs can result in high efficacy of photothermal treatment. To prove this, the cells incubated with 2 mg mL^{-1} ep-Au-MNPs were irradiated by an 808 nm laser with intensities in the range of 250–2000 mW cm^{-2} for 5 min (Fig. 4e). There was no significant cell death from laser irradiation with <500

This journal is © The Royal Society of Chemistry and IChemE 2024
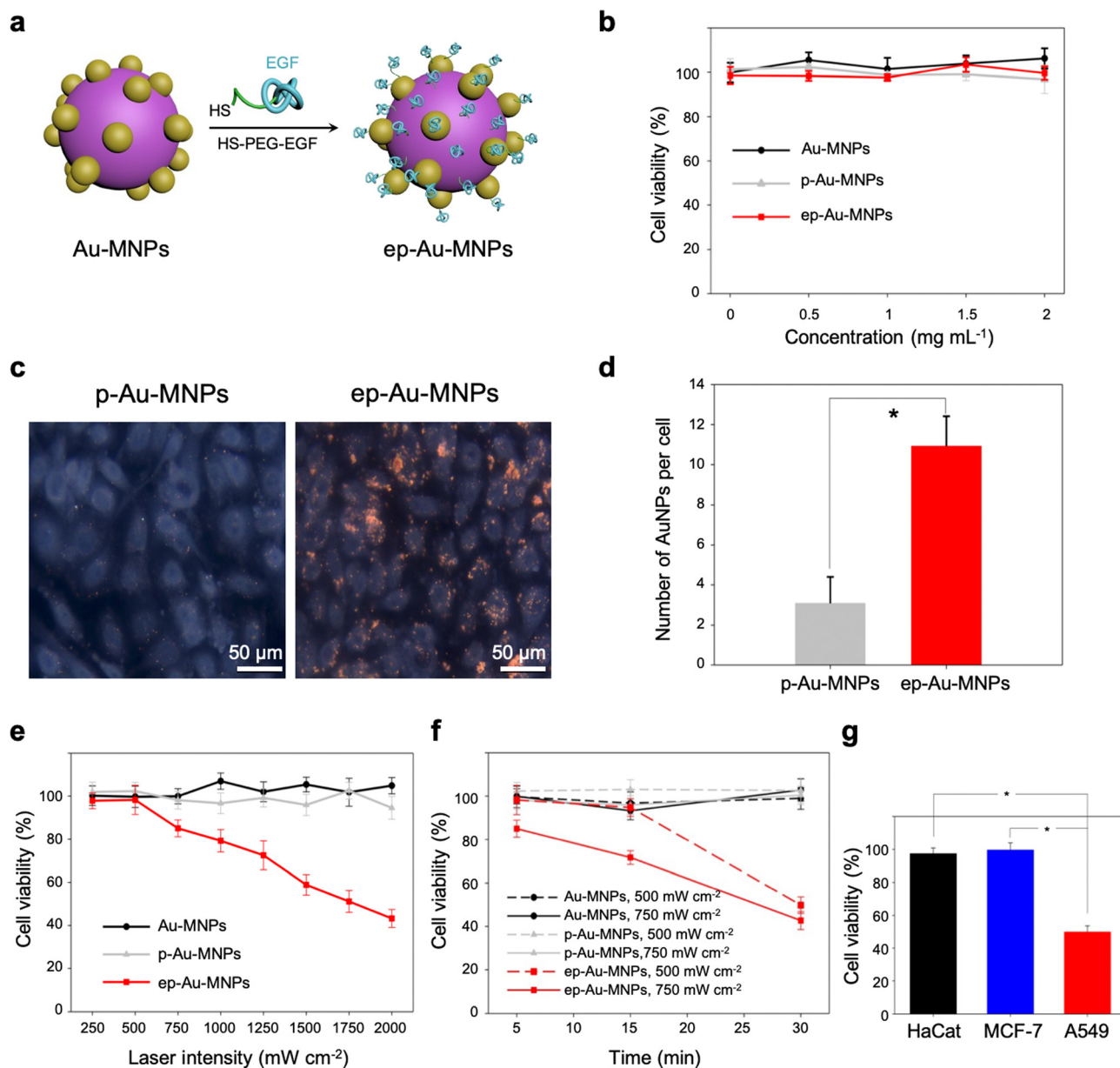
Mol. Syst. Des. Eng., 2024, **9**, 507–517 | **511**

Fig. 4 (a) Schematic to show the functionalization of Au-MNPs with EGF through labeling of AuNPs with the thiolated PEG terminated with EGF (HS–PEG–EGF). (b) Concentration-dependent cytotoxicity of Au-MNPs, p-Au-MNPs, and ep-Au-MNPs evaluated with A549 cells, respectively. (c) Dark-field optical microscopy images of A549 cells treated with p-Au-MNPs and ep-Au-MNPs. (d) The number of AuNPs per cell taken by A549 for p-Au-MNPs and ep-Au-MNPs measured by inductively coupled plasma mass spectrometry (ICP-MS) (*p-value < 0.01). (e) Laser-intensity-dependent cell viability of A549 treated with Au-MNPs, p-Au-MNPs, and ep-Au-MNPs, where the irradiation period was 5 min. (f) Irradiation-period-dependent cell viability of A549 treated with Au-MNPs, p-Au-MNPs, and ep-Au-MNPs, where laser intensities of 500 and 750 mW cm^{-2} are used. (g) Cell viability of three different cell lines of HaCaT, MCF-7, and A549 treated with ep-Au-MNPs at a concentration of 2 mg mL^{-1}, where the cells were irradiated with a laser with an intensity of 500 mW cm^{-2} for 30 min. (*p-value < 0.01).

mW cm^{-2}, and the cell viability decreased with increasing the intensity. The viability was as low as 50% with an intensity of 1750 mW cm^{-2}. For comparison, cell viabilities were inspected of Au-MNPs and p-Au-MNPs under the same conditions. There was almost no cell death over the entire range of intensity, which indicates that cellular uptake is critical for the high efficacy of the photothermal treatment. The period of laser irradiation can also influence the cell viability. For all three nanoparticles, we investigated the influence of the irradiation

period in the range of 5–30 min at two intensities (500 and 750 mW cm^{-2}) (Fig. 4f). Au-MNPs and p-Au-MNPs had a negligible effect on cell viability with both intensities, regardless of the irradiation period, as expected from the low cellular uptake. On the contrary, ep-Au-MNPs showed cell viability as low as 50% with low-intensity (500 mW cm^{-2}) irradiation for 30 min. This is comparable with the result from irradiation at 1750 mW cm^{-1} for 5 min. With the intensity of 750 mW cm^{-2}, irradiation of 15 and 30 min yielded cell viability of 71.6% and 42.7%,

512 | Mol. Syst. Des. Eng., 2024, 9, 507–517

This journal is © The Royal Society of Chemistry and IChemE 2024

respectively. We further studied the cell selectivity of EGF conjugation using two additional cell lines, MCF-7 and HaCaT as they express much less EGF receptors.[39–41] Laser irradiation at the intensity of 500 mW cm^{-2} for 30 min caused little cytotoxic effects for MCF-7 and HaCaT cells: 99.5% and 97.4% cell viability, respectively (Fig. 4g). The results confirm that the cellular internalization is critically important for efficient photothermal therapeutic effects.

To demonstrate the potential of ep-Au-MNPs as *in vivo* tumor-targeted photothermal agents, we used a human xenograft mouse model with A549.[4] It should be noted that, with 808 nm lasers, tissue penetration spans from a few millimeters to one centimeter, affected by the tissue's optical characteristics and the laser's settings. The wavelength falls within the NIR optical window, where biological tissues show reduced absorption, enhancing therapy potential. The targeting efficiency of ep-Au-MNPs was compared with p-Au-MNPs by evaluating the biodistribution after 24 h post-intravenous tail vein injection of 100 μL dispersion with a concentration of 5 mg mL^{-1} of ep-Au-MNPs. Most of the ep-Au-MNPs were accumulated in tumors and the liver, whereas most of the p-Au-MNPs were in the liver, which indicates successful targeting of ep-Au-MNPs to the tumor site (Fig. 5a). After the intravenous injection, the tumor sites in the mice were irradiated with the laser at 1500 mW cm^{-2} for 5 min while monitoring the temperature of the site (Fig. 5b). The temperature increased over time and reached the maximum (48 °C) in 5 min. By contrast, the maximum temperature of the tumor site of mice injected with p-Au-MNPs only reached a maximum of 40 °C. This is comparable with that of mice after PBS injection, indicating no photothermal effect from the nanoparticles. The corresponding photothermal images of mice injected with p-Au-MNPs and ep-Au-MNPs were captured from the FLIR camera, as shown in Fig. S12.† The change in tumor volume was also monitored daily after irradiation, as shown in Fig. 5c. The tumor with ep-Au-MNPs exhibited significant suppression, whereas the tumors with p-Au-MNPs and PBS continued to grow. The laser-irradiated tumor tissues treated with ep-Au-MNPs, which were stained with hematoxylin and eosin (H&E), showed significant necrotic shrinkage of cells and eruption of the extracellular matrix. Local inflammation and signs of edema, which is caused by the heat, are observed in the third panel of Fig. 6, shown by an arrow. In addition, histopathologic examination shows neither damage nor inflammation in harvested organs including the liver, spleen, kidney, heart, and lung (Fig. S13†). Therefore, these results indicate that ep-Au-MNPs can induce photothermal effects to suppress and destroy A549 cells specifically.

Materials and methods

Materials

CM–PEG–SH (MW 5 kDa) was purchased from Laysan Bio, Inc (Arab, AL, USA). Dopamine hydrochloride, EDC, NHS, MES buffer, and HAuCl$_4$, were purchased from Sigma-Aldrich (St. Louis, MO, USA). EGF was provided by Celltrion, Inc.
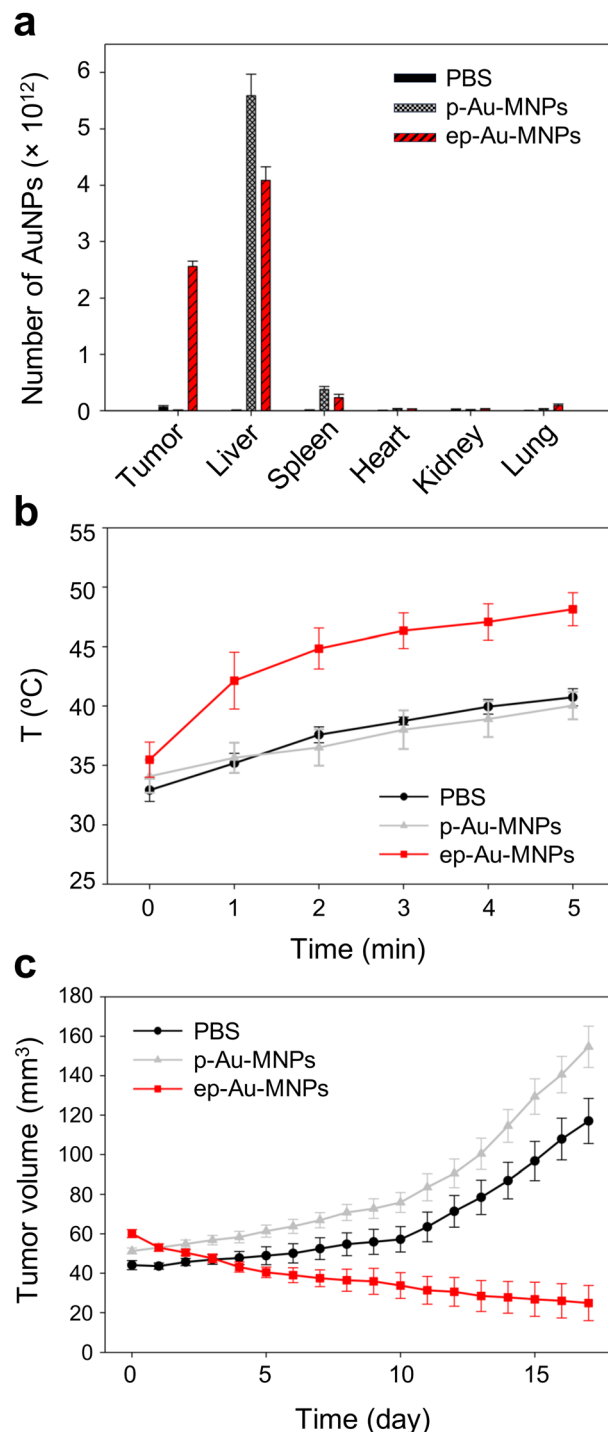

Fig. 5 (a) Biodistribution of Au NPs in a human xenograft mouse model with A549, treated with PBS, p-Au-MNPs, and ep-Au-MNPs, respectively. (b) A temperature change of tumor sites during irradiation of 808 nm laser with an intensity of 1500 mW cm^{-2}, where tumors are treated with PBS, p-Au-MNPs, and ep-Au-MNPs, respectively. (c) Temporal change of tumor volume after irradiation of the laser on day 0, where mice are injected with PBS, p-Au-MNPs, and ep-Au-MNPs, respectively (left).

(Incheon, Republic of Korea). Dulbecco's modified eagle's medium (DMEM) and Roswell Park Memorial Institute
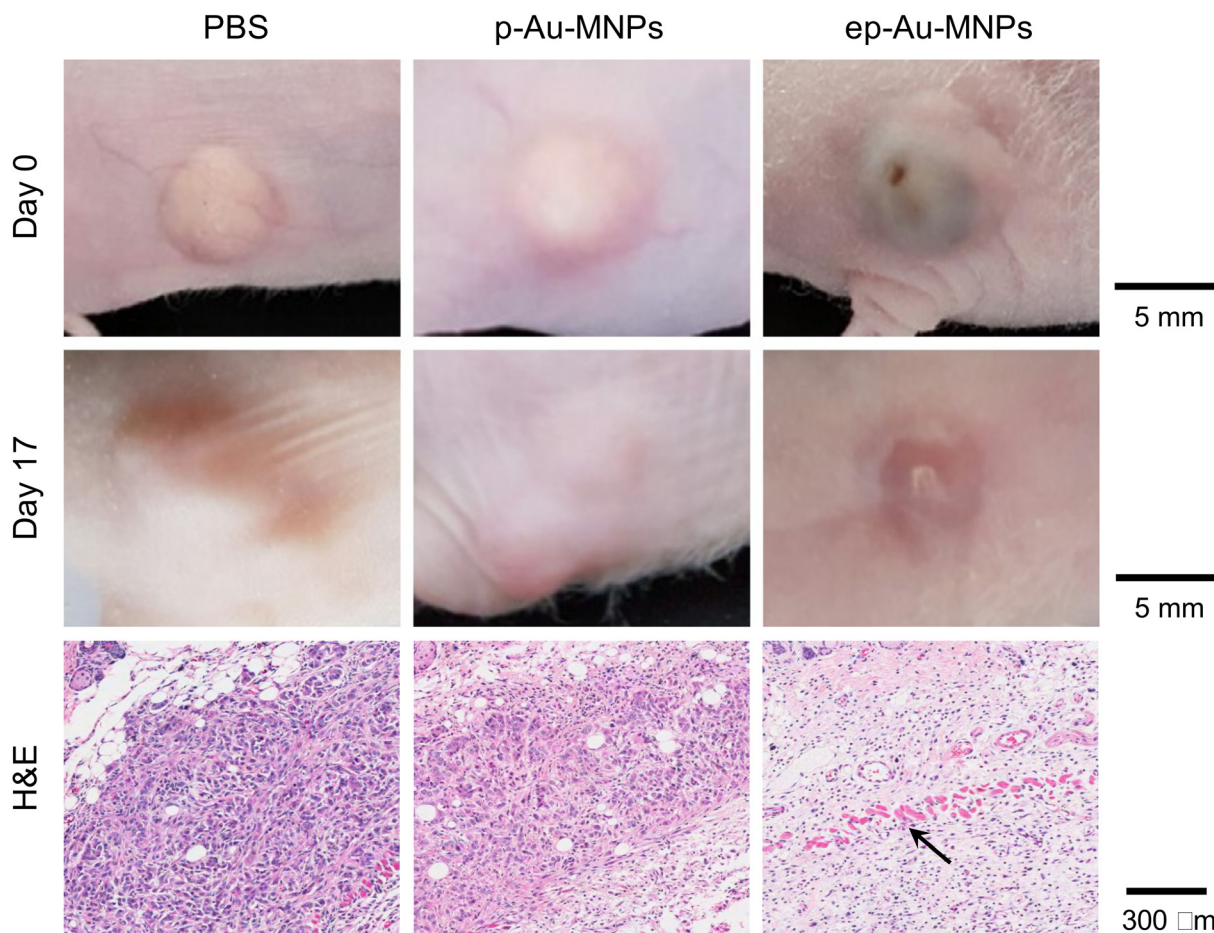
Fig. 6 Digital camera images of tumors in a human xenograft mouse model treated with PBS, p-Au-MNPs, and ep-Au-MNPs, respectively. The photos were taken on day 0 (the first row) and day 17 (the second row) post photothermal treatments. Haematoxylin and eosin (H&E) staining (the third row) of irradiated tumor tissues. The black arrow indicates signs of inflammation and edema.

(RPMI) medium were obtained from Invitrogen (Carlsbad, CA, USA). PBS and FBS were purchased from Thermo Fisher Scientific, Ltd (Waltham, MA, USA). CCK-8 was purchased from Dojindo Laboratories (Kumamoto, Japan).

Synthesis of Au-MNPs

MNPs were first prepared by adding 175 mg of dopamine hydrochloride in 100 mL of deionized water in a round flask at 50 °C. After the dopamine hydrochloride was dissolved, 528 μL of 1 M NaOH was added to the solution and stirred for 3 h at 400 rpm. The prepared MNPs were then centrifuged at 18 000 rpm for 10 min and washed with deionized water three times. The nanoparticles were collected and 200 μL of 1 wt% $HAuCl_4$ was added via a syringe pump (KDS 200, KD Scientific, MA, USA) at a flow rate of 100 μL min^{-1}. This reaction was performed in a round flask at 25 °C for 2 h of continuous stirring at 400 rpm.

Functionalization of au-MNPs with EGF

To functionalize Au-MNPs, EGF-PEG conjugates were initially prepared by adding 5 mg of CM–PEG–SH to 1 mL of 10 mM

MES buffer (pH 5.5), followed by 5 μmol of EDC and NHS for 15 min. Next, 6 mg of EGF was added to the activated PEG for 6 h at 25 °C. The solution was dialyzed using a dialysis membrane (MWC 10 kDa) for 12 h. After preparation of EGF–PEG conjugates, 200 μL of Au-MNPs were mixed with 400 μL of EGF–PEG conjugates for 24 h at 25 °C. The solution was centrifuged (18 000 rpm) for 10 min to remove unbound EGF–PEG conjugates and resuspended in PBS. The conjugation efficiency was determined by measuring the concentrations of EGF–PEG before and after functionalization using a Nanodrop spectrophotometer (ND-1000, DE, USA).

Characterization

The morphology of the nanoparticles was observed with a transmission electron microscope (Tecnai F20, Philips, OR, USA). The elemental analysis was conducted with energy-dispersive X-ray spectroscopy (EDS). The structural configuration and elemental composition were studied using XPS (Sigma Probe, Thermo VG Scientific). FT-IR (ALPHA-P, Bruker Optics, MA, USA) analysis was also conducted to obtain structural information about gold decoration. The

molecular weights of the CM–PEG–SH, EGF, and EGF–PEG conjugates were measured with an MALDI-TOF mass spectrometer (Bruker autoflex III, MA, USA). In addition, RP-HPLC (Agilent 1260 Infinity, CA, USA) was used to measure the retention times of EGF and EGF–PEG molecules. The hydrodynamic diameter and zeta potentials were measured with DLS (ELSZ-1000, Otsuka Electronics Co., Ltd., Osaka, Japan). The absorbance spectra of the nanoparticles were measured using UV-visible light absorption spectroscopy (UV-1800, Shimadzu Corp., Kyoto, Japan). The morphology of the nanoparticles was observed using FE-TEM (Tecnai F20) at an acceleration voltage of 200 kV. The conjugation efficiency was determined by evaluating the concentration of EGF–PEG molecules before and after the functionalization of ep-Au-MNPs. The initial concentration of EGF–PEG molecules was measured as 2.87 mg mL^{-1} and the supernatant concentration of EGF–PEG molecules collected from Au-MNPs was measured after centrifugation (0.07 mg mL^{-1}).

Measurement of photothermal transduction

The photothermal effects were characterized by the temperature increase during 808 nm laser irradiation. Suspensions of MNPs and Au-MNPs in quartz cells were irradiated, and the temperature was recorded with a thermometer.

Serum dispersion stability

Au-MNPs, p-Au-MNPs, and ep-Au-MNPs at the concentration of 2 mg mL^{-1} were incubated with 10% FBS/PBS at 37 °C for 12 h. The hydrodynamic diameters were measured at time intervals of 0, 3, 6, 9, and 12 h using DLS.

Cytotoxicity assay

To determine the cytotoxicity of nanoparticles, A549 cells (1 × 10^4 cells per well) were seeded on a 96-well plate and treated with Au-MNPs, p-Au-MNPs, and ep-Au-MNPs in the concentration range 0–2 mg mL^{-1} for 24 h. The cells were washed with PBS three times to remove excess nanoparticles, and treated with 100 μL of CCK-8 solution for 40 min at 37 °C. The absorbance was measured at 450 nm using a microplate reader (CLARIOstar, BMG Labtech Co., Ltd., Ortenberg, Germany).

Intracellular distribution of nanoparticles

The internalization of nanoparticles in cells was observed using a dark-field microscope (Leica DM1000, Leica Co., Ltd, Wetzlar, Germany). A549 cells (1 × 10^5 cells per chamber) were seeded on a 4-chamber glass slide and not treated with nanoparticles; or exposed to Au-MNPs, p-Au-MNPs, and ep-Au-MNPs at a concentration of 2 mg mL^{-1} for 4 h. The cells were then washed with PBS three times and fixed with 4% formaldehyde. The slide was mounted with VECTASHIELD® as an antifade fluorescent medium and observed under a dark-field microscope. The number of AuNPs inside cells was

measured with ICP-MS (Agilent ICP-MS 7700S). A549 cells (1 × 10^6 cells per well) were seeded in a 6-well plate and treated with p-Au-MNPs and ep-Au-MNPs for 4 h. The cells were then washed with PBS three times. The collected cells were treated with 70% nitric acid to degrade cell membranes before ICP-MS analysis. The number of nanoparticles per cell (N_{Au}) was calculated using the following equation:

$$N_{Au} = \frac{N_{total}}{N} \frac{1}{NC_{total}},\qquad(1)$$

where N_{total} is the number of gold atoms within the cells, N is the average number of gold atoms per nanoparticle, and NC_{total} is the total number of treated cells. The diameter of the gold nanoparticles (D, nm) used in all the experiments was 20 nm. The value of N (3862) was determined using the following equation:

$$N = \frac{\pi \rho D^3}{6} \frac{N_A}{M} N = \frac{\pi \rho D^3}{6} \frac{N_A}{M},\qquad(2)$$

where ρ denotes the density for face-centered cubic (fcc) gold (19.3 g cm^{-3}), M is the atomic mass of gold (197 g mole^{-1}), and N_A is Avogadro's number.[8]

In vitro photothermal effects of nanoparticles

A549 cells (1 × 10^4 cells per well) were seeded in a 96-well plate for 24 h. The cells were then treated with Au-MNPs, p-Au-MNPs, and ep-Au-MNPs at a concentration of 2 mg mL^{-1} for 4 h at 37 °C, washed with PBS three times, and replaced with 100 μL of fresh RPMI media in each well. The cells were irradiated with an 808 nm laser at various intensities in the range 250–2000 mW cm^{-2} and periods in the range 5–30 min. After irradiation, the cells were treated with 100 μL of CCK-8 solution for 40 min at 37 °C. The absorbance was measured at 450 nm using a microplate reader, which was used to calculate cell viability using eqn (1). In addition, cells of the HaCaT and MCF-7 types were seeded in the same manner as for the A549 cells.

Biodistribution and in vivo photothermal effects of nanoparticles

Male SPF/VAF immunodeficient mice were implanted with A549 cells (1 × 10^7 cells per mouse) in the right hind flank of each mouse. The protocol for animal studies was reviewed and approved by the KAIST Institutional Animal Care and Use Committee (KA2015-21). The mice were used for the study of biodistribution and photothermal therapy when the tumors reached an average volume of 45–55 mm^3. For biodistribution, the mice were injected intravenously through the tail with PBS, p-Au-MNPs, and ep-Au-MNPs at a concentration of 5 mg mL^{-1}. Twenty-four hours after injection, the mice were euthanized and the tumor and organs were collected to determine the number of AuNPs by ICP-MS. As for photothermal therapy, mice bearing A549 cells (1 × 10^7 cells per mouse) were injected intravenously through the tail with PBS, p-Au-MNPs, and ep-Au-MNPs at a

This journal is © The Royal Society of Chemistry and IChemE 2024

Mol. Syst. Des. Eng., 2024, **9**, 507–517 | 515

concentration of 5 mg mL^{-1}. Twenty-four hours post-injection, the tumors were irradiated with an 808 nm laser at 1500 mW cm^{-2} for 5 min. The temperature change was recorded with a FLIR T420 thermal camera (FLIR Systems, Inc.). The tumor dimensions were measured with a vernier caliper, and the volume was calculated using eqn (3):

$$V = \frac{\pi}{6} XYZ, \tag{3}$$

where V is the tumor volume (mm^3), X is the tumor width, Y is the tumor length, and Z is the tumor height (mm). For the histology study, fixed organs were embedded in paraffin, sliced, and mounted in ~3 μm-thick sections on microscopic slides. The sections were stained with H&E and analyzed using light microscopy (Leica DMI3000 B, Wetzlar, Germany).

Conclusions

In this work, we demonstrated that melanin-gold hybrid nanoparticles, comprising MNPs decorated with smaller AuNPs, can serve as a promising NIR-active photothermal agent for targeted tumor treatment. Colloidal MNPs of 190 nm in diameter were synthesized by the oxidative polymerization of dopamine, and ~20 nm AuNPs were spontaneously generated on the surface of MNPs. The hybrid nanoparticles exhibited significantly higher NIR light absorption and photothermal conversion compared to MNPs and AuNRs. The surface functionalization with EGF as a targeting ligand enabled efficient cellular uptake and *in vivo* tumor targeting in a xenograft mouse model. Our work highlights two key success factors for localized hyperthermia: (1) how efficiently photothermal nanoparticles 'absorb' NIR and 'convert' the excitonic energy to heat and (2) how efficiently they are delivered to the tumor tissue. Furthermore, biocompatibility and photochemical stability are essential to fulfill the requirements for clinical applications. In this sense, our melanin-gold hybrid nanoparticles hold great promise as viable photothermal agents as they are designed to enhance NIR absorption and photothermal conversion and provide versatile surface chemistry for ligand functionalization and colloidal stabilization.

Author contributions

Conceptualization, Y. S. N., S. H. K.; methodology, G. P., S. C., J. H. Y.; software, G. P.; validation, G. P., J. H. Y.; formal analysis, G. P., S. C., J. H. Y.; investigation, G. P., S. C., J. H. Y.; data curation, G. P., S. C., J. H. Y.; writing – original draft preparation, G. P. and J. H. Y.; writing – review and editing, Y. S. N.; supervision, Y. S. N., S. H. K.; project administration, Y. S. N.; funding acquisition, Y. S. N.

Conflicts of interest

There are no conflicts to declare.

Acknowledgements

References

1 M. Overchuk, R. A. Weersink, B. C. Wilson and G. Zheng, *ACS Nano*, 2023, **17**, 7979–8003.

2 X. Li, J. F. Lovell, J. Yoon and X. Chen, *Nat. Rev. Clin. Oncol.*, 2020, **17**, 657–674.

3 H. Arami, S. Kananian, L. Khalifehzadeh, C. B. Patel, E. Chang, Y. Tanabe, Y. Zeng, S. J. Madsen, M. J. Mandella, A. Natarajan, E. E. Peterson, R. Sinclair, A. S. Y. Poon and S. S. Gambhir, *Nat. Nanotechnol.*, 2022, **17**, 1015–1022.

4 G. L. Seah, J. H. Yu, B. I. Koo, D. J. Lee and Y. S. Nam, *J. Mater. Chem. B*, 2018, **6**, 7737–7749.

5 H. S. Choi, Y. Kim, J. C. Park, M. H. Oh, D. Y. Jeon and Y. S. Nam, *RSC Adv.*, 2015, **5**, 43449–43455.

6 Z. Shi, M. Luo, Q. Huang, C. Ding, W. Wang, Y. Wu, J. Luo, C. Lin, T. Chen, X. Zeng, L. Mei, Y. Zhao and H. Chen, *Nat. Commun.*, 2023, **14**, 6567.

7 B. Geng, D. Yang, D. Pan, L. Wang, F. Zheng, W. Shen, C. Zhang and X. Li, *Carbon*, 2018, **134**, 153–162.

8 M. H. Oh, J. H. Yu, I. Kim and Y. S. Nam, *ACS Appl. Mater. Interfaces*, 2015, **7**, 22578–22586.

9 X. Huang, I. H. El-Sayed, W. Qian and M. A. El-Sayed, *J. Am. Chem. Soc.*, 2006, **128**, 2115–2120.

10 X. C. Jiang, A. Brioude and M. P. Pileni, *Colloids Surf., A*, 2006, **277**, 201–206.

11 B. D. Chithrani, A. A. Ghazani and W. C. W. Chan, *Nano Lett.*, 2006, **6**, 662–668.

12 Y. Liu, K. Ali, J. Liu, M. Deng, Y. He and L. Lu, *Adv. Mater.*, 2013, **25**, 1353–1359.

13 S. Cho and S. H. Kim, *J. Colloid Interface Sci.*, 2015, **458**, 87–93.

14 K. Y. Ju, Y. W. Lee, S. H. Lee, S. B. Park and J. K. Lee, *Biomacromolecules*, 2011, **12**, 625–632.

15 J. Park, H. Moon and S. Hong, *Biomater. Res.*, 2019, **23**, 24.

16 L. Tan, W. Tang, T. Liu, X. Ren, C. Fu, B. Liu, J. Ren and X. Meng, *ACS Appl. Mater. Interfaces*, 2016, **8**, 11237–11245.

17 Y. Tian, S. Shen, J. Feng, X. Jiang and W. Yang, *Adv. Healthcare Mater.*, 2015, **4**, 1009–1014.

18 K. C. L. Black, J. Yi, J. G. Rivera, D. C. Zelasko-Leon and P. B. Messersmith, *Nanomedicine*, 2013, **8**(1), 17–28.

19 L. Zhang, H. Su, J. Cai, D. Cheng, Y. Ma, J. Zhang, C. Zhou, S. Liu, H. Shi, Y. Zhang and C. Zhang, *ACS Nano*, 2016, **10**(11), 10404–10417.

20 Y. Lee, J. Kim, D. S. Yun, Y. S. Nam, Y. Shao-Horn and A. M. Belcher, *Energy Environ. Sci.*, 2012, **5**, 8328–8334.

21 Y. S. Nam, A. P. Magyar, D. Lee, J. W. Kim, H. Park, T. S. Pollom, D. A. Weitz and A. M. Belcher, *Nat. Nanotechnol.*, 2010, **5**, 340–344.

22 I. Kim, H. Y. Son, M. Y. Yang and Y. S. Nam, *ACS Appl. Mater. Interfaces*, 2015, **7**, 14415–14422.

516 | *Mol. Syst. Des. Eng.*, 2024, **9**, 507–517

This journal is © The Royal Society of Chemistry and IChemE 2024

23 H. Y. Son, I. Kim and Y. S. Nam, *J. Ind. Eng. Chem.*, 2015, **30**, 220–224.

24 H. Y. Son, J. H. Ryu, H. S. Lee and Y. S. Nam, *ACS Appl. Mater. Interfaces*, 2013, **5**, 6381–6390.

25 K. R. Kim, J. Kim, J. W. Kim, C. T. Yavuz, M. Y. Yang and Y. S. Nam, *Sep. Purif. Technol.*, 2021, **254**, 117674.

26 H. Y. Son, H. Jun, K. R. Kim, C. A. Hong and Y. S. Nam, *J. Ind. Eng. Chem.*, 2018, **63**, 420–425.

27 A. O. Govorov and H. H. Richardson, *Nano Today*, 2007, **2**, 30–38.

28 J. Kim, K. Lee and Y. S. Nam, *Biotechnol. Bioprocess Eng.*, 2021, **26**, 689–707.

29 H. Y. Son, D. J. Lee, J. B. Lee, C. H. Park, M. Seo, J. Jang, S. J. Kim, M. S. Yoon and Y. S. Nam, *RSC Adv.*, 2014, **4**, 55604–55609.

30 H. Y. Son, K. R. Kim, C. A. Hong and Y. S. Nam, *ACS Omega*, 2018, **3**, 6683–6691.

31 D. K. Roper, W. Ahn and M. Hoepfner, *J. Phys. Chem. C*, 2007, **111**, 3636–3641.

32 C. Li, Z. Liu and P. Yao, *RSC Adv.*, 2016, **6**, 33083–33091.

33 S. Wang, X. Zhao, S. Wang, J. Qian and S. He, *ACS Appl. Mater. Interfaces*, 2016, **8**, 24368–24384.

34 X. Liu, B. Li, F. Fu, K. Xu, R. Zou, Q. Wang, B. Zhang, Z. Chen and H. Junqing, *Dalton Trans.*, 2014, **43**, 11709–11715.

35 H. Zhang, H. Yang, H. J. Chen, X. Du, D. Wen and H. Wu, *Energy*, 2017, **141**, 32–39.

36 S. Choi and Y. S. Nam, *Biosens. Bioelectron.*, 2022, **210**, 114288.

37 W. B. Zhao, J. Park, A.-M. Caminade, S.-J. Jeong, Y. H. Jang, S. O. Kim, J.-P. Majoral, J. Cho and D. H. Kim, *J. Mater. Chem.*, 2009, **19**, 2006–2012.

38 J. Yun, A. N. Cho, S. W. Cho and Y. S. Nam, *Biomater. Sci.*, 2018, **6**, 3388–3396.

39 F. Zhang, S. Wang, L. Yin, Y. Yang, Y. Guan, W. Wang, H. Xu and N. Tao, *Anal. Chem.*, 2015, **87**, 9960–9965.

40 S. Yook, Z. Cai, Y. Lu, M. A. Winnik, J. Pignol and R. M. Reilly, *Mol. Pharmaceutics*, 2015, **12**, 3963–3972.

41 R. M. Reilly, R. Kiarash, J. Sandhu, Y. W. Lee, R. G. Cameron, A. Hendler, K. Vallis and J. Gariépy, *J. Nucl. Med.*, 2000, **41**, 903–911.

This journal is © The Royal Society of Chemistry and IChemE 2024

Mol. Syst. Des. Eng., 2024, **9**, 507–517 | **517**